NUCL SCI TECH (2020) 31:116
https://doi.org/10.1007/s41365-020-00822-6

Corrosion assessment for spent nuclear fuel disposal in crystalline rock, using variant cases of hydrogeological modeling

Chi-Che Hung[1] · Fraser King[2] · Yun-Chen Yu[1] · Chi-Jen Chen[1] · Yuan-Chieh Wu[1] · Wei-Ting Lin[3]

Received: 10 July 2020 / Revised: 10 September 2020 / Accepted: 14 September 2020 / Published online: 3 December 2020

Abstract This paper presents a corrosion assessment of copper spent nuclear fuel disposal canisters in crystalline rock, using hydrogeological modeling. A simplified approach is considered, to avoid complex and time-consuming computer simulations. This simplified case is presented as a base case, with changes in the hydrogeological parameters presented as variant cases. The results show that in Taiwan's base case, decreasing the hydraulic conductivity of the rock or decreasing the hydraulic conductivity of dikes results in a shorter transport path for sulfide and an increase in corrosion depth. However, the estimated canister failure time is still over one million years in the variant cases.

Keywords Spent nuclear fuel disposal · Corrosion assessment · Hydrogeological modeling

1 Introduction

The Taiwan Power Company (Taipower) is currently in the process of demonstrating the feasibility and capability of deep geological disposal of the country's spent nuclear fuel. The current concept is based on the Swedish KBS-3 approach, suitably modified for Taiwanese conditions. In collaboration with the Institute of Nuclear Energy Research (INER), a reference case is being developed to demonstrate the feasibility of the concept, as part of the Feasibility Assessment Report for the Spent Nuclear Fuel Final Disposal Technology in Taiwan (abbreviated as "SNFD2017"). The disposal facilities are designed on the principle of using crystalline rock as a natural barrier. The sub-surface facilities consist of engineered barriers (copper shell canister, buffer, backfill, closure, and plug) around the underground disposal locations. The floor of the deposition tunnel is designed at 500 m depth. The nearest distance between the repository and the Taiwushan fault is 350 m, and the Taiwushan fault-branch is at least 550 m away. The alignment of the deposition tunnel is perpendicular to a dolerite dike, and the distance between dike and repository is 100 m. The repository has a total of 62 tunnels. Each disposal tunnel is 300 m in length and can accommodate 44 deposition holes [1].

In any geological disposal environment, the canister will be subject to corrosion, and it is necessary to assess the rate and extent of corrosion over long periods of time, with the aim of confirming the primary safety function of the canister, avoiding the release of the internal nucleus.

Corrosion assessment lists the primary corrosion processes that occur in a repository environment. These processes are categorized into limited corrosion and long-term corrosion. The corrosion effects due to radiolysis of air and

This work was supported by the Taiwan Power Company (TPC) (No. 0780509001).

✉ Wei-Ting Lin
wtlin@niu.edu.tw

[1] https://www.iner.gov.tw

[2] https://www.prci.org/Research/PRCIDirectory/9974.aspx

[3] https://www.niu.edu.tw

water, as well as corrosion by atmospheric air before repository closure, are considered to be limited corrosion, as the processes are temporary. Corrosion processes resulting from oxygen trapped in the repository in the initial period after closure, the sulfide content of the pyrites, and the sulfide generated by sulfate-reducing bacteria, belong to the category of limited corrosion because the total quantity of the corrodent is limited. Once the repository reaches anoxic conditions, the primary source of corrodent is the groundwater that continuously carries corrosive substances to the surfaces of the canisters by means of diffusion, infiltration, or advection, which is deemed a long-term corrosion process. Once the corrodent reaches the surface of the canister, the corrosion reaction rate is assumed to be infinitely fast. Thus, the quantity of corrodent can be calculated by chemical mass balance to directly obtain the amount of corrosion.

When conducting a corrosion assessment, the first step is to calculate the corrosion depth of each limited corrosion process; the next is to thereby obtain the remaining thickness of the copper shell, and the final step is to obtain the long-term corrosion rate to assess the containment failure time for each canister. With regard to the limited corrosion processes, the amount of corrodent in each case is calculated in accordance with the cause of the corrosion, and then chemical mass balance is used to obtain the corrosion depth. For the long-term corrosion processes, the corrosion rates can be calculated from data obtained by the discrete fracture network (DFN) model simulation, and it is necessary to consider two scenarios: intact buffer material, and eroded buffer material conditions.

The results of the limited corrosion processes are listed in Table 1. The total quantity of the corrodent generated by the radiolysis of air is estimated based on the radiation dose and half-lives. The copper shell corrosion depth that corresponds to the general corrosion on the sides of the canisters is 1.3×10^{-6} mm. As for the radiolysis of water, the volume of irradiated water is calculated by reference to the canister design, indicating that the total quantity of corrodent and the corresponding thickness of the corrosion depth is 1.10×10^{-2} mm. The canisters are assumed to be placed in the repository environment for three years before repository closure. The oxygen content in the atmosphere that exists prior to the closure causes corrosion of these canisters; the corresponding corrosion depth is 1.50×10^{-3} mm. Regarding the oxygen trapped in the repository in the initial period immediately after the closure, the respective volumes of pores in the backfill and buffer are calculated by referring to the repository design, where the oxygen content in the air reaches the surfaces of the canisters by means of diffusion, resulting in a corrosion depth of 1.02×10^{-1} mm. With regard to the corrosion effect of sulfide from pyrite in the backfill and buffer, the sulfide-induced corrosion depth is estimated to be 1.14×10^{-1} mm based on the sulfide content, solubility, and diffusion coefficient of the sulfide in the buffer. With respect to the sulfide generated by sulfate-reducing bacteria, an estimate based on the experimental results from Masurat et al. [2] corresponds to a copper shell corrosion depth of 1.77×10^{-6} mm. The total corrosion depth as a result of these limited corrosion processes is estimated to be less than 1 mm.

For long-term corrosion processes, scenarios including both intact buffers and eroded buffers are considered. However, as protected by the intact buffer, the canisters have between one hundred thousand years and one million years of service life. Therefore, in this study, the corrosion assessment focuses on the eroded buffer scenario. Because the total corrosion depth of the limited processes amounts to 0.41 mm, and incorporates the variation that occurs in the copper shell production process, a remaining copper shell thickness of 47 mm is conservatively assumed for the eroded buffer corrosion assessment. A maximum sulfide ion concentration in the groundwater of 5.4×10^{-6} mol/L was used for the reference case.

Table 1 Estimated depth of corrosion after one million years for the various limited corrosion processes considered in the assessment

Corrosion processes	Assessment method	Corrosion depth (mm)
Radiolysis of moist air in canister-buffer gap	Mass balance based on G-value for HNO_3	0.0000013
Radiolysis of water	Mass balance based on G-values for radiolytic oxidants	0.011
Atmospheric	Empirical atm. corrosion rate	0.0015
Initially entrapped oxygen	Mass balance	0.102
Sulfide from pyrite in buffer and backfill	Mass transport (mass balance)	0.114
Sulfide from sulfate reducing bacteria in buffer and backfill	Empirical rates of SO_4^{2-} duction in highly compacted bentonite	0.177

2 Hydrogeological modeling

Because the flow characteristics of groundwater are an important factor for the migration of radionuclides [3], the safety assessment should explore different geosphere transport properties. The reference case is based on a test area on a Taiwanese offshore island with crystalline rock. The west side of the island has the highest terrain (262 m), indicating that the groundwater will flow from this area to the surrounding areas. It is assumed that the west side of the test area is defined as a no-flow boundary according to Carnahan et al. [4] and Davis [5]. The flow rate of groundwater decreases with increasing depth. The base of the rock mass is assumed to act as a no-flow boundary, and the remaining boundary conditions will have different settings in different cases, as shown in Fig. 1. The basic information for the Taiwan Reference Case is provided by a geological investigation of the K-area, which is part of the offshore island. The K-area is approximately 10 km wide from east to west, and 15 km long from north to south. The information on the model domain included surface topography, the depth of the bottom boundary, and the geometry and position of four types of hydraulic units: regolith, intact rock, major water-conducting features, and flow barrier structures. The Taiwushan fault and branch fault are two of the major water conducting features, and the eleven dikes (of 100 m width and 1000 m spacing) are assumed to be flow barriers. The computational grid, shown in Fig. 1, is a horizontal cut plane of the grid at $z = -504$ m. DarcyTools has the ability to generate unstructured grids, so the refinement is applied from the default cell size (128 m × 128 m × 128 m) by setting a maximum cell size (32 m × 32 m × 32 m) in the Taiwushan fault, the branch fault, the eleven dikes, and on the top of the domain. Then, the grid is globally refined in the repository zone (8 m × 8 m × 8 m), and more restrictively around the main tunnel and deposition tunnel (1 m × 1 m × 1 m) and deposition holes (0.5 m × 0.5 m × 0.5 m). Finally, successive refinements lead to a total of 8618,037 cells. Because all of the cases in

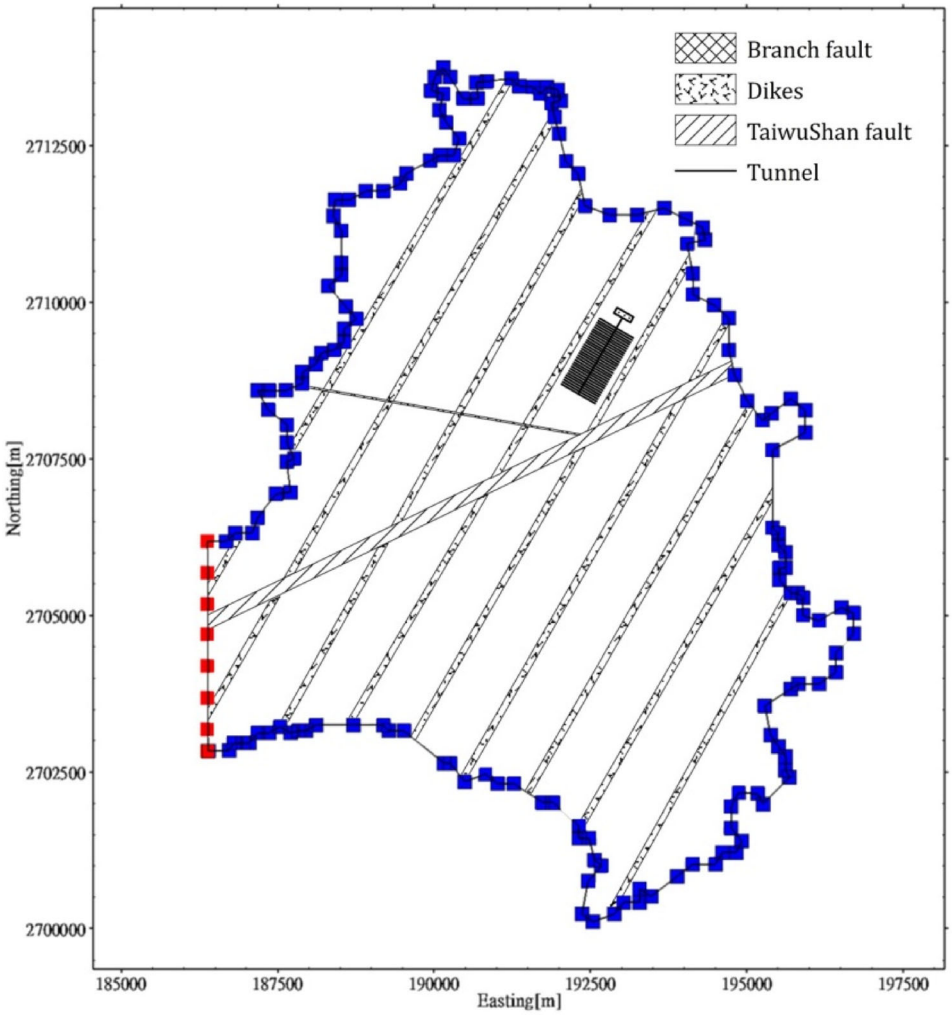

Fig. 1 (Color online) Model domain with fault zone and regularly-spaced dikes

this study are steady-state, the initial conditions are not quite critical. Therefore, we do not assign the initial conditions in all cases. Regarding the domain size and boundary conditions, the bedrock hydrogeology directly assumes that the depth of the bottom boundary is − 2000 m. The top of the domain is described by the digital terrain model with 30 m resolution, which is also provided by the Reference Case. The boundary is assigned either as a specified head (implying a freshwater head equal to the elevation of the ground surface) or a specified recharge of 35 mm/year, depending on the particular case. As for the lateral boundary conditions, the western side, which is demonstrated by red rectangular symbols, is assumed to be a no-flow boundary, while the remaining parts of the lateral boundary, which are demonstrated by blue rectangular symbols, can be assigned as either specified head boundary conditions (implying a head equal to sea level) or no-flow boundary conditions, depending on the particular case.

The hydrogeological model uses the continuous method to treat the fractured rock mass as a continuous-pore-type medium. Many scholars use local geological survey data, including ground and geochemical data, to construct three-dimensional numerical models for petroleum development, geothermal resource exploration, and groundwater resource protection [6–8]. Because the range of fracture length scales ranges from meters to kilometers, the accurate prediction of the flow and solute transport behavior of fractured rock formations requires the acquisition of local fracture-related parameters, the generation of discrete fracture networks, and appropriate equivalent parameter conversion techniques [9, 10]. A DFN model based on the hydrogeological information of the reference case and the Swedish SKB experience [11–15] is shown in Fig. 2. Using DFN up-scaling to equivalent continuous porous medium (ECPM) mode, a series of groundwater flow simulation case studies and performance measures (PMs) were performed. The final results are used for the near-field corrosion and far-field radionuclide transport assessments. In this study, we focus on the impact of hydrogeological simulation results on corrosion assessment in various cases. Figure 2 shows a fragment of the total fracture systems that intersect the repository. The repository is composed of a main tunnel, deposition tunnels, and deposition holes. Fractures are described with square planer for DFN generation. Connectivity analysis is performed before up-scaling the hydraulic properties of fractures into effective hydraulic parameters in each grid. This figure is an example of connectivity analysis after DFN generation. The deep blue fractures represent the conducting fractures that will be retained for the subsequent calculation of effective hydraulic properties, while the gray fractures will

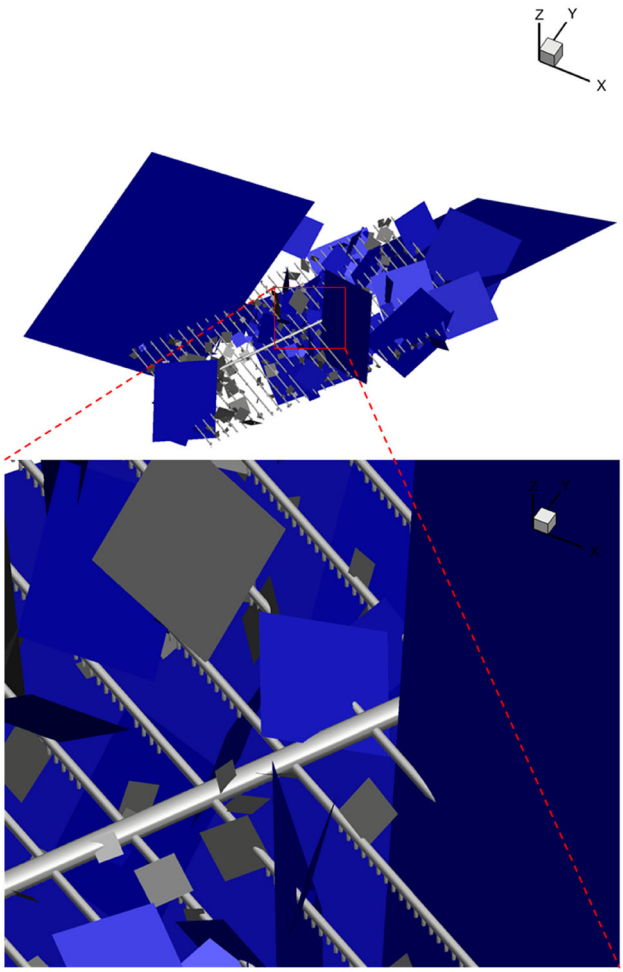

Fig. 2 (Color online) Example realization using the DFN model. The deep blue shows fracture-connected water flow; the light blue shows isolated fractures with no flow

be removed because they are single fractures or isolated clusters that have no contribution to flow.

The hydrogeological model was built using DarcyTools for use in relation to subsequent radionuclide transport and calculations for all the deposition holes. DarcyTools is a simulation program developed jointly by SKB (Svensk Karnbranslehantering AB), MFRDC (Michel Ferry, R & D Consulting), and CFE AB (Computer-aided Fluid Engineering AB) for simulating flow in porous and fractured media.

To fully understand the deep groundwater migration, it is necessary to determine the hydrogeological characteristics of the deep formation and to understand the physical properties of the treatment of the rock, and then to construct a hydrogeological conceptual model to facilitate the subsequent groundwater simulation. Therefore, a series of groundwater flow simulation cases are established to illustrate the assumptions, boundary settings, and simulation results of different cases. In the current sea-level

model, Case O is defined as the original case of the reference case. Because of the effect of adding salinity and density-driven flow, Case O is complex and consumes enormous computer simulation time and resources. In order to increase the efficiency of the operation without losing authenticity, four cases were implemented for the simplified settings represented by Cases A to D. In these four cases, the effects of salinity are ignored, with different boundary conditions used to simulate the density flow effect of Case O. The case in which the simulation results are most similar to Case O will be referred to as the base case for the subsequent series of analyses.

The base case will be used to execute the other three cases related to the hydrogeological characterization parameters, where the base case will be re-represented in Case 1, and the remaining cases will be expressed in Cases 2 to 4. Table 2 shows the assumptions for all cases.

Case O is mainly used to simulate the true situation of the groundwater flow field in the test area, and therefore includes salinity (salinity of seawater is set to 3.2%) and the effect of density flow. The top boundary condition sets the ground surface to a fixed pressure of 0 (indicating that the freshwater head is the same as the surface elevation). Except for the west side, which is set to no flow, the remaining lateral boundary conditions are set to the net water pressure of the seawater. The bottom is also assumed to be a no-flow boundary.

The remaining lateral boundary condition of Case A is set as the freshwater head (hydrostatic state); the top boundary assumes a specified net recharge of 35 mm/year, which is based on precipitation and evapotranspiration calculations; the bottom is still set to be a no-flow boundary.

Case B has the same top boundary condition as Case A, assuming a specified net recharge of 35 mm/year. The remaining lateral boundary condition of the domain is assumed to be a no-flow boundary (i.e., including the west); the bottom is also a no-flow boundary condition. The boundary condition of this case assumes that the interface between freshwater and seawater below the island can be appropriately modeled as an impervious boundary.

The lateral boundary of Case C is set to the same freshwater supply head (hydrostatic state) as Case A; the top boundary is assumed to be the same as the surface

Table 2 The boundary conditions (BCs) of the 8 cases

Case	Density	Top BC	Lateral BC	Comment
O	Variable	Salinity = 0% Hydrostatic pressure = 0 Pa	Salinity = 3.2% Hydrostatic pressure of seawater head	Original case with salinity; intended to represent realistic conditions with regard to density-driven flow
A	Constant	Salinity = 0% Net recharge flow rate = 35 mm/year	Salinity = 0% Hydrostatic pressure of freshwater head	Simplified model without salinity; to test whether the imposed BCs can make the model mimic the Original case (Case O). Recharge top BC
B	Constant	Salinity = 0% Net recharge flow rate = 35 mm/year	Salinity = 0% Net recharge flow rate = 0 mm/year	Simplified model without salinity; to test whether the imposed BCs can make the model mimic the Original case (Case O). Recharge top BC
C	Constant	Salinity = 0% Hydrostatic pressure = 0 Pa	Salinity = 0% Hydrostatic pressure of freshwater head	Simplified model without salinity; to test whether the imposed BCs can make the model mimic the Original case (Case O)
D and 1	Constant	Salinity = 0% hydrostatic pressure = 0 Pa	Salinity = 0% net recharge flow rate = 0 mm/year	Simplified model without salinity; to test whether the imposed BCs can make the model mimic the Original case (Case O) The case using geological survey data at Reference case and considering the maximum [HS-] at 500 m depth
2	Constant	Salinity = 0% Hydrostatic pressure = 0 Pa	Salinity = 0% Net recharge flow rate = 0 mm/year	Generally, both fracture frequency and permeability decrease with depth. To test the sensitivity of flow and transport to a step change, this case is run where the hydraulic conductivity below − 700 m is reduced to 10^{-12} m/s
3	Constant	Salinity = 0% Hydrostatic pressure = 0 Pa	Salinity = 0% Net recharge flow rate = 0 mm/year	Dikes are generally believed to be of lower permeability than the surrounding rock. This variant case is run where the conductivity is lowered by one order of magnitude to 10^{-12} m/s
4	Constant	Salinity = 0% Hydrostatic pressure = 0 Pa	Salinity = 0% Net recharge flow rate = 0 mm/year	This case is a combination of the Cases 2 and 3 above. The hydraulic conductivity is below − 700 m, and dikes are reduced to 10^{-12} m/s

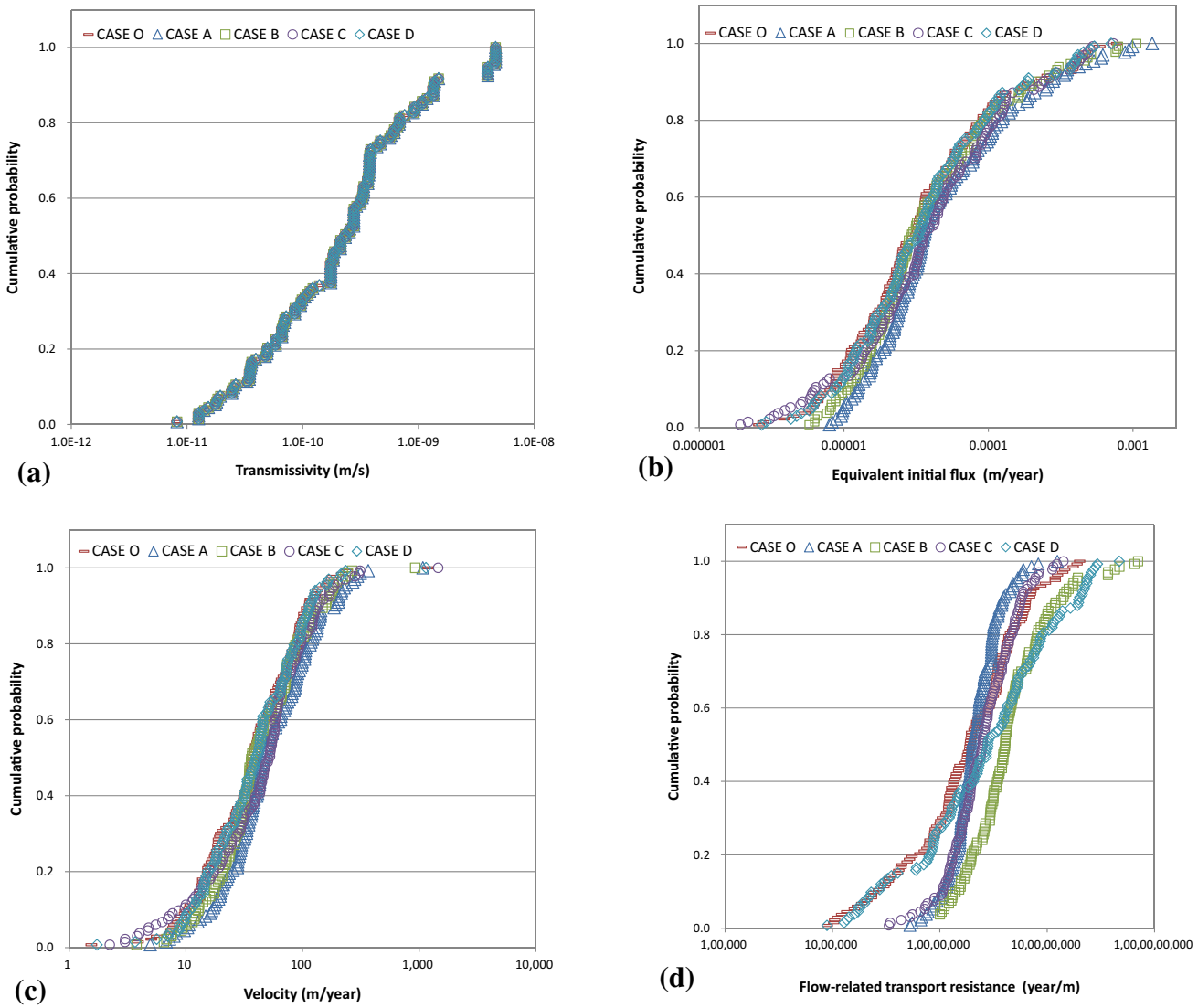

Fig. 3 (Color online) **a** Cumulative distribution functions (CDFs) of transmissivity for Case O, Case A, Case B, Case C, and Case D; **b** CDFs of equivalent initial flux for Case O, Case A, Case B, Case C, and Case D; **c** CDFs of velocity for Case O, Case A, Case B, Case C, and Case D; **d** CDFs of flow-related transport resistance for Case O, Case A, Case B, Case C, and Case D

topographic elevation (the same as the top boundary of Case O); the west lateral boundary is still a no-flow boundary, and the bottom is still set as a no-flow boundary.

The top boundary of Case D is the fixed hydrostatic pressure; the lateral boundary is set to no flow, including the west lateral boundary, and the bottom is also assumed to be a no-flow boundary.

According to evidence from Sweden on fractured rock masses [16], the fracture frequency and permeability of the rock decrease with depth. This trend is presented in terms of continuity or step characteristics. Therefore, Case 2 assumes that the hydraulic conductivity of the rock below − 700 m will be reduced from 10^{-11} to 10^{-12} m/s.

Case 3 sets the hydraulic conductivity of the dikes to 10^{-12} m/s because the dikes generally have a lower permeability than the surrounding rocks.

Case 4 is a combination of the hydrogeological conditions of Case 2 and Case 3. It is also assumed that the hydraulic conductivities of the rock and all dikes below − 700 m are reduced to 10^{-12} m/s.

3 Eroded bentonite methodology

Chemical erosion of the bentonite results in a loss of material and a reduction in density, with a corresponding increase in hydraulic conductivity and the possibility of advective transport in the buffer. The methodology used for

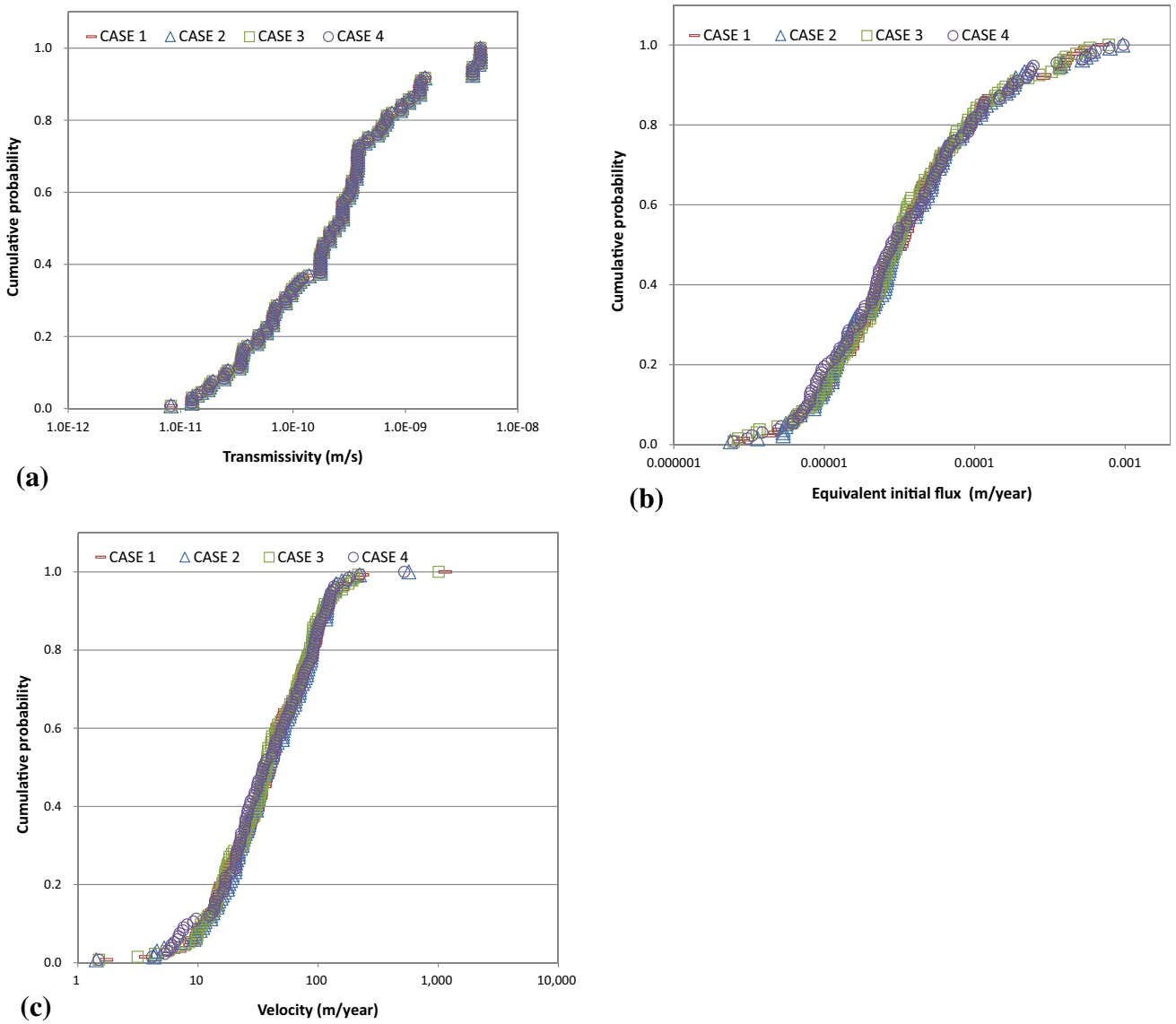

Fig. 4 (Color online) **a** CDFs of transmissivity for Case 1, Case 2, Case 3, and Case 4; **b** CDFs of equivalent initial flux for Case 1, Case 2, Case 3, and Case 4; **c** CDFs of velocity for Case 1, Case 2, Case 3, and Case 4

the assessment of the extent of corrosion of copper canisters in the case of eroded bentonite follows very closely that developed by SKB, and is described in more detail by SKB [17], the Taiwan Power Company [18], and Hung et al. [1]. Briefly, the time taken to achieve advective transport conditions in the buffer (t_{adv}) is estimated from the montmorillonite release rate ($R_{Erosion}$) from

$$t_{adv} = \frac{m_{buffadv}}{R_{Erosion} f_{tdilute}}, \quad (1)$$

where $m_{buffadv}$ is the amount of buffer that must be removed to allow advection, and $f_{tdilute}$ is the fraction of time that the dilute water that promotes bentonite dissolution is present.

Once advective conditions have been established, the equivalent groundwater flow rate (Q_{eq}) that determines the supply of sulfide to the canister surface is given by either the flux through that part of the fracture assumed to intersect the deposition hole (q_{eb}) or, for high flow rates, by

$$Q_{eq} = 1.13 \frac{\sqrt{q_{eb} D_w V_{zone}}}{d_{buffer}}, \quad (2)$$

where D_w is the diffusivity of sulfide in water, V_{zone} is the volume of eroded buffer, and d_{buffer} is the buffer thickness. The corrosion rate is then estimated based on the equivalent flow rate, the concentration of sulfide in the groundwater, and the stoichiometry of the corrosion reaction

$$2Cu + HS^- + H_2O = Cu_2S + H_2 + OH^- \quad (3)$$

.

4 Base case simplified from the original case

Because Case O contains the effects of salinity and density flow, the simulation time and computing resources are significant. In order to increase the computational efficiency without losing authenticity, four cases neglecting the influence of salinity, and with different boundary conditions set, were implemented. The purpose is to obtain a simplified flow path similar to Case O. The simplified case serves as a base case and is used for subsequent hydrogeological parameter variation in the variant case simulations. In the safety assessment, transmissivity (T), water velocity (V) and equivalent initial flux (U) will, respectively, affect the erosion of the buffer material and the corrosion of the canisters. The flow-related transport resistance (F) is a measure of the resistance to transport in the far field.

In order to facilitate the study of variability, the same DFN realization is used in this study. Figure 3a shows the cumulative distribution functions (CDFs) of transmissivity in Case O and Cases A to D. In the same DFN realization, the deposition holes of different boundary cases will present the same trend of transmissivity. As shown in Fig. 3b, the CDFs of the initial equivalent flux in Case O and Cases A to D are very similar, and the flux for Case D is almost the same as that for Case O. However, the cases where the upper boundary is a constant pressure (Cases C and D) have lower values. Figure 3c shows the CDFs of water velocity crossing the deposition hole for Case O and Cases A to D. This trend is similar to the trend of equivalent initial flux, and the difference between the two is mainly because the water velocity refers to the flow rate in the fracture, and the equivalent initial flux refers to the flux in the deposition hole. The water velocity in the fracture varies due to the degree of conductivity of each deposition hole, resulting in varying degrees of equivalent initial flux change. Figure 3d shows the CDFs of the water flow transmission impedance of Case O and Cases A to D, from which it can be seen that the results of Case D are the most widely distributed, probably due to the fact that the spatial distribution of the surface release is most common. In addition, when the cases with water no-flow boundaries (Cases B and D) are compared to those with hydrostatic boundaries (Cases A and C), the flow-related transport resistance distribution range is wider in the former than in the latter. Based on the flow-related transport resistance of the different analyses, Case D is selected as the base case, as a simplified version of the original case. In addition, it is of general interest to investigate methods for simplification, so that complicated modeling does not take an unnecessary part of the computer resources available. This is also consistent with previous studies [19, 20].

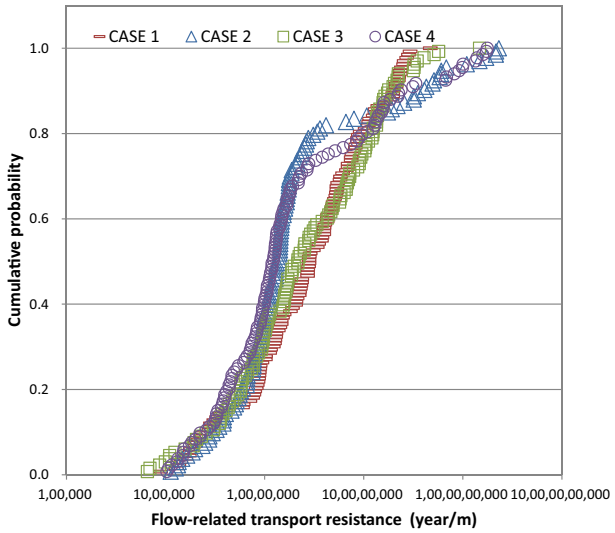

Fig. 5 (Color online) CDFs of flow-related transport resistance for Case 1, Case 2, Case 3 and Case 4

5 Corrosion scenario case analysis results

After obtaining a simplified base case similar to Case O in terms of its hydrogeological parameters, the base case will be renumbered as Case 1. Different hydrogeological

Table 3 Predicted bentonite erosion times and resulting extent of corrosion in the case of eroded bentonite for the five deposition holes with the highest corrosion rates in Case 1

Dep. hole ID	Flow-rate (m^3/year)	Erosion time (year)	Corrosion depth in 10^6 years (mm)[a]	Failure time (year)
DH-631	0.0119	1.61×10^5	1.74	$> 10^6$
DH-121	0.0092	1.79×10^5	1.41	$> 10^6$
DH-2712	0.0086	1.85×10^5	1.35	$> 10^6$
DH-2594	0.0077	2.01×10^5	1.23	$> 10^6$
DH-1433	0.0071	1.99×10^5	1.16	$> 10^6$

[a]Including 0.41 mm corrosion in 10^6 years due to the limited corrosion processes in Table 1. Assuming a wall thickness of 47 mm and groundwater sulfide concentration of 5.4×10^{-6} mol/L

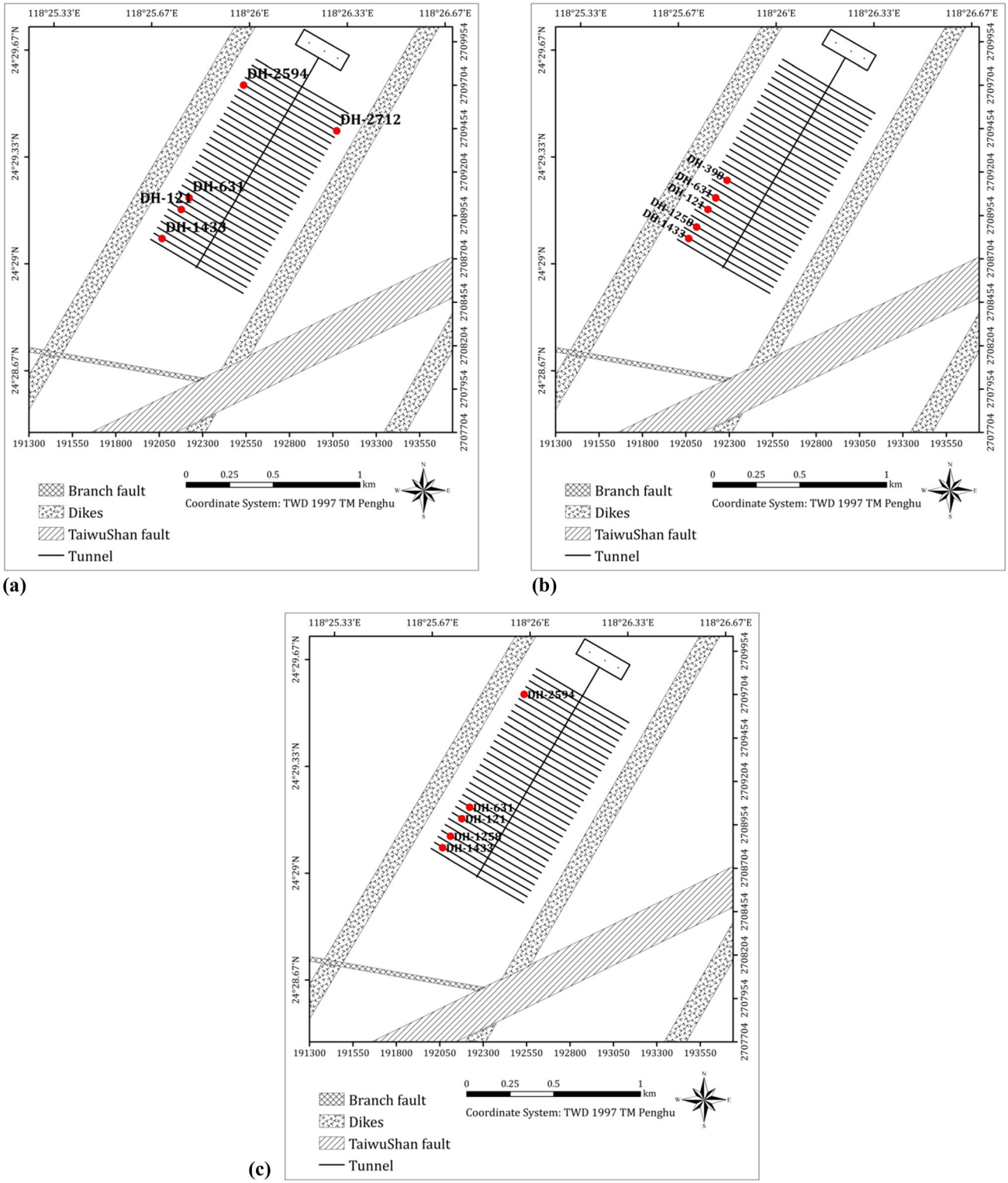

Fig. 6 **a** The deposition hole locations with the five highest copper corrosion rates for Case 1; **b** the deposition hole locations with the five highest copper corrosion rates for Cases 2 and 4; **c** the deposition hole locations with the five highest copper corrosion rates for Case 3

parameter settings will result in different pressure distributions or particle transfer flow fields. Thus, three different hydrogeological variant cases were selected for the dikes and rock. Compared with Case 1, Case 2 decreases the hydraulic conductivity of the rock, Case 3 decreases the hydraulic conductivity of dikes, and Case 4 decreases both.

Table 4 Predicted bentonite erosion times and resulting extent of corrosion in the case of eroded bentonite for the five deposition holes with the highest corrosion rates in Case 2

Dep. hole ID	Flow-rate (m^3/year)	Erosion time (year)	Corrosion depth in 10^6 years (mm)[a]	Failure time (year)
DH-631	0.0163	1.41×10^5	2.27	$> 10^6$
DH-121	0.0134	1.53×10^5	1.92	$> 10^6$
DH-1433	0.0104	1.70×10^5	1.56	$> 10^6$
DH-1258	0.0100	1.72×10^5	1.51	$> 10^6$
DH-398	0.0093	1.78×10^5	1.42	$> 10^6$

[a]Including 0.41 mm corrosion in 10^6 years due to the limited corrosion processes in Table 1. Assuming a wall thickness of 47 mm and groundwater sulfide concentration of 5.4×10^{-6} mol/L

Table 5 Predicted bentonite erosion times and resulting extent of corrosion in the case of eroded bentonite for the five deposition holes with the highest corrosion rates in Case 3

Dep. hole ID	Flow-rate (m^3/year)	Erosion time (year)	Corrosion depth in 10^6 years (mm)[a]	Failure time (year)
DH-631	0.0132	1.54×10^5	1.89	$> 10^6$
DH-121	0.0099	1.74×10^5	1.49	$> 10^6$
DH-1433	0.0092	1.79×10^5	1.41	$> 10^6$
DH-1258	0.0080	1.89×10^5	1.28	$> 10^6$
DH-2594	0.0069	2.11×10^5	1.13	$> 10^6$

[a]Including 0.41 mm corrosion in 10^6 years due to the limited corrosion processes in Table 1. Assuming a wall thickness of 47 mm and groundwater sulfide concentration of 5.4×10^{-6} mol/L

Table 6 Predicted bentonite erosion times and resulting extent of corrosion in the case of eroded bentonite for the five deposition holes with the highest corrosion rates in Case 4

Dep. hole ID	Flow-rate (m^3/year)	Erosion time (year)	Corrosion depth in 10^6 years (mm)[a]	Failure time (year)
DH-631	0.0165	1.41×10^5	2.29	$> 10^6$
DH-121	0.0133	1.54×10^5	1.91	$> 10^6$
DH-1433	0.0108	1.68×10^5	1.60	$> 10^6$
DH-1258	0.0100	1.73×10^5	1.51	$> 10^6$
DH-398	0.0092	1.78×10^5	1.41	$> 10^6$

[a]Including 0.41 mm corrosion in 10^6 years due to the limited corrosion processes in Table 1

To facilitate the discussion of the base case and variant cases, the same trend of transmissivity is predicted, as shown in Fig. 4a. Figure 4b shows the equivalent initial flux result for Cases 1 to 4. Because the change in hydrogeological parameters does not modify the characteristics of the repository, the equivalent initial flux of the deposition hole has a similar trend, and there are also similar results for water velocity, as shown in Fig. 4c.

Assuming a wall thickness of 47 mm and groundwater sulfide concentration of 5.4×10^{-6} mol/L.

However, Fig. 5 shows that the flow-related transport resistance of Case 1 is larger than that of Cases 2 to 4. The hydrogeological parameters of Cases 2 to 4 affect the hydrogeological characteristics of the geologic parameters, shortening the flow path and lowering the flow-related transport resistance. In particular, the values of flow-related transport resistance are significantly reduced in Case 2 and Case 4 due to the lower hydraulic conductivity of the rock. Table 3 shows the bentonite erosion times, corrosion depths after 10^6 years, and failure times in the case of eroded bentonite, for the five deposition holes with the highest corrosion rates in Case 1. The corrosion depth after 10^6 years includes 0.41 mm due to the limited corrosion processes. The copper thickness was assumed to be 47 mm, and the groundwater sulfide concentration was set at 5.4×10^{-6} mol/L. The locations of the five deposition holes with the highest corrosion rates in Case 1, resulting from the five highest values of Q_{eq}, are shown in Fig. 6a.

The variant cases use the same assumptions for the corrosion assessment. The results are shown in Tables 4, 5 and 6 for Cases 2, 3, and 4, respectively. Cases 2 and 4 have the same five deposition holes with the highest corrosion rates; their locations are shown in Fig. 6b. Figure 6c shows the locations of those in Case 3. In the results of the corrosion assessment, the erosion times of the variant cases were slightly less than that of the base case, due to the impact of erosion time parameters, mainly water velocity and transmissivity. Therefore, decreasing the hydraulic conductivity of the rock and of the dikes results in a greater amount of erosion and a shorter time to establish advective flow conditions. This indicates that the corrosion evaluation is an important index for the current study, and this is also consistent with previous studies [21–23].

In Case 2 and Case 4, all hydraulic conductivity values below − 700 m depth are changed from $1E^{-10}$ to $1E^{-12}$ m/s to reflect the fracture frequency, and the permeability of the rock decreases with depth. In Case 3, the hydraulic conductivity of the dikes is changed from $1E^{-11}$ to $1E^{-12}$ m/s to represent the fact that the permeability of dikes is generally lower than that of rock. The step decrease in hydraulic conductivity of rock in Case 2 results in fewer deep flow paths, since the interface at − 700 m depth will act like a wall. This results in shorter flow paths, and generally increases the flow velocity at the depth of the repository. The same occurs in Case 4.

The main impact on the corrosion rate is due to the equivalent initial flux. Although the equivalent initial fluxes of the variant cases are very similar, their corrosion depths are slightly greater than the corrosion depth of the base case, especially for Cases 2 and 4. In the absence of the limited corrosion processes, the top five corrosion depths are approximately 23% to 51% higher than the base case. In the case of decreased hydraulic conductivity of the dikes, the top five corrosion depths of Case 3 are increased by approximately − 4 to 11% compared with the base case. However, the canister failure time is still over one million years.

6 Conclusion

In Taiwan's base case, decreasing the hydraulic conductivity of the rock or of the dike formations below − 700 m increases the flow rate due to a decrease in the hydraulic conductivity above this depth, resulting in a shorter transport path for sulfide and an increase in the corrosion depth. This indicates that the corrosive agents are more likely to be transported to the surface of the canisters to cause corrosion. This study has investigated methods to simplify the complicated hydrogeological modeling, and the simplified modeling is suitable for use in the corrosion assessment of spent nuclear fuel disposal systems. With the current evaluation method, the main influence on corrosion is shown to be the equivalent initial flux. Nevertheless, the results of the corrosion assessment show that the canister failure time is still over one million years for all the variant cases.

References

1. C.C. Hung, Y.C. Wu, F. King, Corrosion assessment of canister for the disposal of spent nuclear fuel in crystalline rock in Taiwan. Corros. Eng. Sci. Technol. **52**, 194–199 (2017). https://doi.org/10.1080/1478422X.2017.1285855
2. P. Masurat, S. Eriksson, K. Pedersen, Microbial sulphide production in compacted Wyoming bentonite MX-80 under in situ conditions relevant to a repository for high-level radioactive waste. Appl. Clay Sci. **47**, 58–64 (2010). https://doi.org/10.1016/j.clay.2009.01.004
3. JNC: H12:Project to establish the scientific and technical basis for HLW disposal in Japan, Project overview report. Japan Nuclear Cycle Development Institute, JNC-T21410-2000-001 (2000). https://www.jaea.go.jp/04/tisou/english/report/H12_report.html
4. B. Carnahan, H.A. Luther, J.O. Wilkes, *Applied Numerical Methods* (Wiley, Hoboken, 1969)
5. M.E. Davis, *Numerical Methods and Modeling for Chemical Engineers* (Wiley, Hoboken, 1984)
6. S.E. Gasda, J.M. Nordbotten, M.A. Celia, Application of simplified models to CO_2 migration and immobilization in large-scale geological systems. Int. J. Greenh. Gas Control **9**, 72–84 (2012). https://doi.org/10.1016/j.ijggc.2012.03.001
7. P.J. Quental, J.A. Almeida, M. Simões, Construction of high-resolution stochastic geological models and optimal upscaling to a simplified layer-type hydrogeological model. Adv. Water Resour. **39**, 18–32 (2012). https://doi.org/10.1016/j.advwatres.2012.01.001
8. M. Raiber, P.A. White, C.J. Daughney et al., Three-dimensional geological modelling and multivariate statistical analysis of water chemistry data to analyse and visualise aquifer structure and groundwater composition in the Wairau Plain, Marlborough District, New Zealand. J. Hydrol. **436–437**, 13–34 (2012). https://doi.org/10.1016/j.jhydrol.2012.01.045
9. P.M. Adler, J.F. Thovert, *Fractures and Fracture Networks* (Springer, Berlin, 1999). https://doi.org/10.1007/978-94-017-1599-7
10. E.P. Nelson, A.J. Kullman, M.H. Gardner, et al., Fault-Fracture Networks and Related Fluid Flow and Sealing, Brushy Canyon Formation, West Texas, Faults and Subsurface Fluid Flow in the Shallow Crust, American Geophysical Union (2013). https://agupubs.onlinelibrary.wiley.com/doi/10.1029/GM113p0069
11. U. Svensson, M. Ferry, DarcyTools, Version 3.4. User's guide. Swedish Nuclear Fuel and Waste Management Company Report, Svensk Kärnbränslehantering AB, SKB R-10-72 (2010). https://inis.iaea.org/collection/NCLCollectionStore/_Public/42/096/42096525.pdf
12. U. Svensson, M. Ferry: H.O. Kuylenstierna, DarcyTools Version 3.4—concepts, methods andequations. Swedish Nuclear Fuel and Waste Management Company Report, Svensk Karnbranslehantering AB (2010). https://inis.iaea.org/collection/NCLCollectionStore/_Public/43/026/43026212.pdf

13. U. Svensson, A Laboratory scale analysis of groundwater flow and salinity distribution in the Aspo area. Swedish Nuclear Fuel and Waste Management Company Report, Svensk Karnbranslehantering AB, SKB TR-99-24 (1999). https://inis.iaea.org/collection/NCLCollectionStore/_Public/31/018/31018541.pdf
14. U. Svensson, Aspo Hard Rock Laboratory. Prototype Repository, Groundwater flow, pressure and salinity distributions around the Prototype Repository. Continuum model No 1. Swedish Nuclear Fuel and Waste Management Company Report, Svensk Karnbranslehantering AB, SKB IPR-01-40 (2001). http://www.skb.com/pub/19079/ipr-01-40.pdf
15. U. Svensson, DarcyTools Version 3.4. Verification, validation and demonstration. Swedish Nuclear Fuel and Waste Management Company Report, Svensk Karnbranslehantering AB, SKB R-10-71 (2010). http://www.skb.com/publication/2217100/R-10-71.pdf
16. S. Follin, Bedrock hydrogeology Forsmark. Site descriptive modelling, SDM-Site Forsmark. Swedish Nuclear Fuel and Waste Management Company Report, Svensk Kärnbränslehantering AB, SKB R-08-95 (2008). https://www.skb.se/publication/1877175/R-08-95.pdf
17. SKB: Corrosion calculations report for the safety assessment SR-Site, Swedish Nuclear Fuel and Waste Management Company Report, Svensk Kärnbränslehantering AB, SKB TR 10-66 (2010). https://www.skb.se/publikation/2192376/TR-10-66.pdf
18. Taiwan Power Company: Feasibility assessment report for the spent nuclear fuel final disposal technology in Taiwan. Main report. Taiwan Power Company, Taipei, Taiwan (2016). https://www.aec.gov.tw/webpage/control/waste/files/index_06_f1.pdf
19. Q. Wang, H. Li, W. Zheng et al., Model analysis of the influence of coolant impurity on the properties of high temperature alloys of HTGR. Nucl. Tech. **43**(4), 040006 (2020). https://doi.org/10.11889/j.0253-3219.2020.hjs.43.040006. (**in Chinese**)
20. X. Zhang, A. Shang, Study on LOCA accident of fuel rod with SiCf/SiC cladding. Nucl. Tech. **42**(8), 080601 (2019). https://doi.org/10.11889/j.0253-3219.2019.hjs.42.080601. (**in Chinese**)
21. X. Wang, J. Zhang, Y. Chen et al., Effects of water radiolysis on corrosion rate of 316 stainless steel in reactors. Nucl. Tech. **43**(8), 080002 (2020). https://doi.org/10.11889/j.0253-3219.2020.hjs.43.080002. (**in Chinese**)
22. Q. Guo, J. Zhang, Y. Chen, Calculation and analysis of activated corrosion products of multi-phase in water cooling loops under fusion reactor. Nucl. Tech. **42**(6), 060602 (2019). https://doi.org/10.11889/j.0253-3219.2019.hjs.42.060602. (**in Chinese**)
23. G. Lei, S. Yang, R. Liu et al., The effect of He bubbles on the corrosion properties of nickel-based alloy in molten salt environment. Nucl. Tech. **42**(4), 040602 (2019). https://doi.org/10.11889/j.0253-3219.2019.hjs.42.040602. (**in Chinese**)